Classical and Quantum Gravity

PAPER • **OPEN ACCESS**

The primordial magnetic field in our cosmic backyard

To cite this article: Sebastian Hutschenreuter *et al* 2018 *Class. Quantum Grav.* **35** 154001

View the article online for updates and enhancements.

Related content

- The origin, evolution and signatures of primordial magnetic fields
  Kandaswamy Subramanian
- Cosmological Structure Formation and Magnetic Fields
  E. R. Siegel and J. N. Fry
- Cosmological backgrounds of gravitational waves
  Chiara Caprini and Daniel G Figueroa

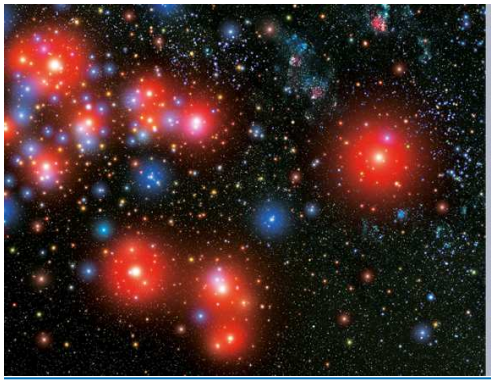

IOP Astronomy ebooks

Part of your publishing universe and your first choice for astronomy, astrophysics, solar physics and planetary science ebooks.

iopscience.org/books/aas

OPEN ACCESS
IOP Publishing
Classical and Quantum Gravity
Class. Quantum Grav. **35** (2018) 154001 (24pp)
https://doi.org/10.1088/1361-6382/aacde0

The primordial magnetic field in our cosmic backyard

Sebastian Hutschenreuter[1,2,10], Sebastian Dorn[1,2], Jens Jasche[3], Franco Vazza[4,5,6], Daniela Paoletti[7,8], Guilhem Lavaux[9] and Torsten A Enßlin[1,2]

[1] Max Planck Institute for Astrophysics, Karl-Schwarzschildstr.1, 85741 Garching, Germany
[2] Ludwig-Maximilians-Universität München, Geschwister-Scholl-Platz 1, 80539 Munich, Germany
[3] Department of Physics, Stockholm University, Albanova University Center, SE 106 91 Stockholm, Sweden
[4] University of Bologna, Department of Physics and Astronomy, Via Gobetti 93/2, I-40129, Bologna, Italy
[5] Universität Hamburg, Hamburger Sternwarte, Gojenbergsweg 112, 40129, Hamburg, Germany
[6] Istituto di Radioastronomia, INAF, Via Gobetti 101, 40129 Bologna, Italy
[7] INAF/OAS Bologna, Via Gobetti 101, I-40129 Bologna, Italy
[8] INFN, Sezione di Bologna, via Irnerio 46, I-40127 Bologna, Italy
[9] Sorbonne Université & CNRS, UMR 7095, Institut d'Astrophysique de Paris, 98 bis bd Arago, 75014 Paris, France

E-mail: hutsch@mpa-garching.mpg.de

Received 7 March 2018, revised 18 June 2018
Accepted for publication 20 June 2018
Published 16 July 2018

Abstract

We reconstruct for the first time the three dimensional structure of magnetic fields on cosmological scales, which were seeded by density perturbations during the radiation dominated epoch of the Universe and later on were evolved by structure formation. To achieve this goal, we rely on three dimensional initial density fields inferred from the 2M++ galaxy compilation via the Bayesian BORG algorithm. Using those, we estimate the magnetogenesis by the so called Harrison mechanism. This effect produced magnetic fields exploiting the different photon drag on electrons and ions in vortical motions, which are exited due to second order perturbation effects in the Early Universe. Subsequently we study the evolution of these seed fields through the non-

[10] Author to whom any correspondence should be addressed.

Original content from this work may be used under the terms of the Creative Commons Attribution 3.0 licence. Any further distribution of this work must maintain attribution to the author(s) and the title of the work, journal citation and DOI.

linear cosmic structure formation by virtue of a magneto-hydrodynamics simulation to obtain a 3D estimate for the structure of this primordial magnetic field component today. At recombination we obtain large scale magnetic field strengths around 10^{-23}G, with a power spectrum peaking at about 2 Mpc^{-1} h in comoving scales. At present we expect this evolved primordial field to have strengths above $\approx 10^{-27}$ G and $\approx 10^{-29}$ G in clusters of galaxies and voids, respectively. We also calculate the corresponding Faraday rotation measure map and show the magnetic field morphology and strength for specific objects of the Local Universe. These results provide a reliable lower limit on the primordial component of the magnetic fields in these structures.

Keywords: cosmology, primordial magnetic fields, large scale structure, MHD simulations

(Some figures may appear in colour only in the online journal)

1. Introduction

Inference of primordial magnetic fields opens a unique window into the Early Universe between inflation and recombination. Although a variety of different astrophysical processes may generate magnetic fields, the primordial magnetic seed may very well be the origin of observed magnetic fields in galaxies and clusters. Primordial magnetic fields are a viable candidate for the 10^{-16} G to $\approx 10^{-15}$ G [1–4] fields expected in cosmic voids due to the non-observation of GeV emission from TeV blazars among other explanations [5]. In any case, they represent by definition the minimal amount of magnetic fields present in the Universe. Literature provides a variety of very diverse effects for the generation of primordial magnetic fields coherent on a large range of scales. A incomplete list of possible magnetogenesis effects may include mechanisms at the end of inflation (e.g. during the reheating phase or exploiting the electroweak phase transitions), during QCD phase transitions or effects that make use of speculative non-standard model physics such as gravitational coupling of the gauge potential or string theory effects. Very often these mechanisms struggle with producing the necessary field strengths and/or, especially the post inflationary models, the necessary coherence lengths for large-scale magnetic fields. The scale problem might be solved, at least for helical magnetic fields, via an inverse cascade which transfers magnetic power to larger scales [6, 7]. Recent works have shown that a similar mechanism exists for non-helical fields [8], although the process is still poorly understood [9]. For a further discussion on different magnetogenesis models, we refer the reader to comprehensive review articles [10–13].

A more conservative Ansatz solely relying on the assumption of a ΛCDM Universe and conventional plasma physics was proposed by Matarrese *et al* [14]. This approach is based on a mechanism initially proposed by Harrison [15] in 1970. During the later phases of the radiation dominated epoch of the Universe a two fluid battery effect occurred between the proton fluid and the tightly coupled electron-photon fluid. The densities $\rho_{(\alpha)}$, with $\alpha \in \{m, \gamma\}$ for baryons and the electron-photon fluid respectively, of the two components scale with the scale factor $a(t)$ as $\rho_{(\mathrm{m})} \sim a(t)^{-3}$ and $\rho_{(\gamma)} \sim a(t)^{-4}$, respectively. Therefore, the separately conserved angular momenta $L_{(\alpha)} \sim \rho_{(\alpha)}\, \omega_{(\alpha)}\, r^5$ in a rotational setup with radius $r(t) \sim a(t)$ requires the angular velocities $\omega_{(\alpha)}$ to depend on $a(t)$ with $\omega_{(\mathrm{m})} \sim a^{-2}$ and $\omega_{(\gamma)} \sim a^{-1}$, respectively. In other words, protons spin down faster than electrons, as the latter are carried by the still dominant photons. This difference in rotation then leads to currents that induce magnetic

fields [15]. The necessary vortical motion of both proton and radiation fluid are caused by effects that can be expressed as second order perturbations of the fluid equation [14].

The recent progress on the inference of the actual 3D realization of the large-scale dark matter structure and its formation history in the Local Universe and the fact that the Harrison mechanism is solely founded on well established plasma physics allows us to calculate the seed magnetic fields that had to be generated by this effect as well as their present day morphology and strength. Since these fields have to exist today in combination with fields of other sources, we are therefore able to provide credible lower bounds on the primordial magnetic field strength in the nearby Universe. We structure this article as following: section 2 first describes the outcome of the Matarrese paper [14] and then presents the computational steps that take us from dark matter over densities to magnetic fields. Section 3 gives a short overview on the dark matter density reconstruction used in this work. Section 5 provides the intermediate results on magnetic field configuration and power spectrum at radiation matter equality. Section 4 shows the results of the subsequent magneto-hydrodynamics (MHD) simulation. Section 6 contains a summary and an outlook on potential improvements.

2. Theory

This paper strongly relies on the theoretical framework outlined by Matarrese *et al* [14]. This approach describes primordial density perturbations in the Early Universe before the recombination epoch as sources of magnetic fields via the Harrison mechanism [15].

In the first part of this section we will summarize their assumptions and results. The second part describes the implemented reconstruction approach to translate our knowledge on dark matter over-densities into magnetic field estimates, first described by Dorn [16].

2.1. Basics

All calculations here are performed using the standard ΛCDM model assuming the cosmological parameters described in table 1 following the 2015 results of the Planck mission [17].

Following [14] we further assume that the dominant constituents of the Universe in the relevant time frame behave as perfect fluids of dark matter, electrons, protons and photons. All equations and calculations are performed in Poisson gauge with the following line element:

$$\mathrm{d}s^2 = a^2(\eta)\left(-(1+2\phi)\,\mathrm{d}\eta^2 + 2\chi_i\, d\eta\,\mathrm{d}x^i + \left((1-2\psi)\,\delta_{ij} + \chi_{ij}\right)\mathrm{d}x^i\mathrm{d}x^j\right) \tag{1}$$

a is the scale factor depending on conformal time η. ϕ and ψ are the Bardeen potentials, χ_i and χ_{ij} are vector and tensor perturbations, respectively.

The perfect fluid assumption results in a vanishing anisotropic stress tensor, which yields $\phi = \psi \equiv \varphi$ to first order in perturbation theory.

As perfect fluids are assumed, the energy momentum tensor simplifies to

$$T_\nu^{(\alpha)\mu} = \left(P^{(\alpha)} + \rho^{(\alpha)}\right) u^{(\alpha)\mu} u_{(\alpha)\nu} + P^{(\alpha)}\delta_\nu^\mu \tag{2}$$

with $P^{(\alpha)}$ the pressure, ρ_α the density and u_α^μ the bulk velocity for each component α. Pressure and density of a component are related via an equation of state

$$P^{(\alpha)} = w^{(\alpha)}\,\rho^{(\alpha)}. \tag{3}$$

We define the energy over-density with respect to the mean energy density $\overline{\rho^{(\alpha)}}$ (which is the same quantity as $\rho_0^{(\alpha)}$ in [14]) of a component as

Table 1. Table of cosmological parameters used in this work [17].

Parameter	Value
H_0	$67.74\,\mathrm{km\,Mpc^{-1}s^{-1}}$
h	0.6774
Ω_Λ	0.6911
Ω_m	0.3089
Ω_r	$5.389 \cdot 10^{-5}$
Ω_k	0.0
z_{eq}	3371

$$\delta^{(\alpha)} = \frac{\rho^{(\alpha)}}{\bar{\rho}^{(\alpha)}} - 1. \tag{4}$$

All quantities $(\delta^{(\alpha)}, u^{(\alpha)}, \varphi, \chi_i, \chi_{ij})$ can now be perturbed up to second order and related via their respective momentum equations including source terms to describe interactions. The coupling between the baryonic and radiation components is assessed by a tight coupling approximation to zeroth order which implies $v_i^{(p)} \approx v_i^{(e)} \approx v_i^{(\gamma)}$. This sets Thomson and Coulomb interaction terms to zero in this order. The curl of the momentum equations for the proton and photon components of the fluid gives evolution equations for the respective vorticities. The magnetic fields will be generated by vortical structures in the conductive non-relativistic baryonic component. To understand this, however, we turn our eye to the dominating photon component in that fluid. If a fluid component α was considered separately, its vorticity $\omega^{(\alpha)}$ is a conserved quantity as stated by Kelvin's circulation theorem. This holds for each order of perturbation theory separately, in particular for the dominating photons:

$$\omega'^{(\gamma)} = 0. \tag{5}$$

Given that we expect no vorticity in the initial conditions, external sources are absent and we have an ideal fluid where pressure and density gradients are aligned, photon vorticity will always be zero. There is however a subtelty that that comes into play due to the fact that photons experience pressure. The photon vorticity equation in second order is [14]

$$\omega_{i\,(2)}^{(\gamma)} = -\frac{1}{2a^2}\epsilon_{ijk}\left[a v_{(2)}^{j,k\,(\gamma)} + a\chi_{(2)}^{j,k} + v_{(1)}^{j\,(\gamma)}\varphi_{(1)}^{,k} + v_{(1)}'^{j\,(\gamma)} v_{(1)}^{k\,(\gamma)}\right]. \tag{6}$$

The vorticity of photons in second order perturbation is not equal to the curl of the second order perturbed velocity field, but includes coupled first order terms. Since we need to obey the conservation law in equation (5) and these first order terms are non-zero, a curl in the photon velocity field needs to be induced. If we now turn our eye to the proton vorticity equation these squared first order terms are absent due to the vanishing pressure:

$$\omega_{i\,(2)}^{(\mathrm{p})} = -\frac{1}{2a}\epsilon_{ijk}\left[v_{(2)}^{j,k\,(\mathrm{p})} + \chi_{(2)}^{j,k}\right]. \tag{7}$$

The crucial connection is now that the tight coupling of the fluid components does not couple the vorticities of protons and photons but their velocities. Therefore the right part in equation (7) is non-zero and acts as a external source term for vorticity. Connecting this with Maxwells equations, we get an equation for the generation of magnetic fields. In other words

the arising proton vorticity needs to be offset by an external (magnetic) force, in order to keep angular momentum conserved. The tight coupling approximation is discussed in more detail in 2.3.

Matarrese *et al* [14] expressed the evolution equation for the magnetic field in terms of the first order scalar perturbations of the metric $\varphi_{(1)}$ which in the Newtonian limit gives the gravitational potential. By assuming negligible resistivity and therefore omitting magnetic diffusion terms and performing (at least partially) an analytic integration, they get [14, 16]

$$B = -\frac{m_p}{e\,a\mathcal{H}^2}\left[2\nabla\varphi' \times \nabla\varphi - \frac{1}{12\mathcal{H}}\nabla\left(\Delta\varphi\right) \times \nabla\varphi - \frac{1}{12\mathcal{H}^2}\nabla\left(\Delta\varphi'\right) \times \nabla\varphi\right] - \frac{1}{a^2}\int_{\eta_I}^{\eta} \mathrm{d}\tilde{\eta}\,\frac{a}{\mathcal{H}}\,\nabla\varphi' \times \nabla\varphi + \frac{a_I^2}{a^2}B_I \tag{8}$$

for the magnetic field at time η, assuming some initial field B_I at time η_I. A prime denotes derivation by conformal time. m_p is the proton mass, e the elementary charge, a the scale factor and $\mathcal{H} = a'/a$ the comoving Hubble constant. In the formulation above, the generation of magnetic fields is the result of a coupling between first order temporal and spatial gradients of the scalar perturbations. In other words, the generation of magnetic fields is the result of dynamics in the gravitational potential, which in turn are a result of the gravitational pull on infalling matter through the horizon and the counteracting radiation pressure. This close connection to the Baryon Accoustic Oscillations (BAOs) will be evident in the power spectra of our results at recombination. Even for $\varphi' = 0$, which is true in the matter dominated era, this terms is not zero, as the second term only depends on spatial gradients. The formulation above is very convenient, as the sole dependence on the scalar perturbations makes the connection to initial conditions and the corresponding state of the Universe today very easy, as will be demonstrated in the next section. Furthermore all terms in equation (8) include at least two derivatives of φ. For large scales above the horizon scales this implies a scaling of the magnetic field power spectrum of approximately k^4. Similar arguments where brought up in [18]. This is also in accordance with the causality limit on uncorrelated magnetic fields, which demands at least a k^2 scaling [19]. The integral term was omitted by Mataresse in their analysis on the correlation structure of the field. The initial field B_I can safely be set to zero due to the a_I^2/a^2 factor. The assumption of small resistivity can be justified via considering the diffusion timescale

$$\tau_{\mathrm{diff}} = 4\pi\sigma L^2, \tag{9}$$

where L typical scale of magnetic structures and σ is the electron conductivity. Electron momentum transfer is dominated via Thomson scattering, we can therefore write $\sigma = \frac{n_e e^2}{n_\gamma m_e \sigma_T}$. Plugging everything in, using the cosmological parameters from the Planck mission [17] e.g. at recombination and $L \approx 1\,\mathrm{Mpc}$, yields

$$\tau_{\mathrm{diff}} \approx 10^{42}\ \mathrm{s}, \tag{10}$$

which is orders of magnitude higher than the age of the Universe at $t_{\mathrm{U}} \approx 4.4 \cdot 10^{17}\mathrm{s}$. Therefore neglecting the diffusion term is justified. In general, this is true throughout the history of the Universe, at least after inflation and on large scales [20]. High conductivity also implies flux freezing, which will lead to field amplification during structure formation in the late time evolution of the magnetic field as we will see in our results.

In the following we discuss the implementation of equation (8).

2.2. Implementation

We now need to calculate φ and its spatial and temporal derivatives with respect to conformal time. We begin our calculation by translating the CDM density perturbations measured[11] shortly before the last scattering surface $\delta_{\mathrm{cdm}}(z \approx 1000)$ into primordial initial conditions deep inside the radiation epoch at z_{p}. Magnetogenesis can only take place on scales which have entered the cosmic horizon at the corresponding epoch. Therefore it makes sense to make this the criterion for z_{p}. We know that the horizon condition can be roughly written as

$$k_{\mathrm{h}} \cdot \eta_{\mathrm{h}} \approx 1 \tag{11}$$

with the conformal time measured in units of one over length, the speed of light set to one and with η indicating conformal time. Knowing that the smallest scales of the grid correspond to $k_{256} \approx 2.39\ \mathrm{h\ Mpc}^{-1}$ and $k_{512} \approx 4.78\ \mathrm{h\ Mpc}^{-1}$ with respective grid sizes of 256 and 512 points respectively, we know that the initial times must be on the order of the grid resolution $\eta_{256} \approx 0.42\ \mathrm{Mpc\ h}^{-1}$ and $\eta_{512} \approx 0.21\ \mathrm{Mpc\ h}^{-1}$ with the speed of light set to one. The equivalent redshifts are $z_{256} \approx 9.7 \cdot 10^5$ and $z_{512} \approx 1.9 \cdot 10^6$. Finally, $z_{\mathrm{p}} = 10^7$ was adopted in this work, as it safely satisfies the aforementioned condition. We obtain $\delta_{\mathrm{cdm}}(z_{\mathrm{p}})$ by using linear cosmological transfer functions and calculate the total energy over-densities $\delta_{\mathrm{tot}}(z_{\mathrm{p}})$ from it,

$$\delta_{\mathrm{tot}}(z_{\mathrm{p}}) = \frac{4}{3}\delta_{\mathrm{cdm}}(z_{\mathrm{p}}) = \frac{4}{3}T(k, z_{\mathrm{p}}, z_{\mathrm{rec}})\,\delta_{\mathrm{cdm}}(z_{\mathrm{rec}}). \tag{12}$$

The 4/3 factor comes from the adiabatic super-horizon solutions for the density perturbations (see e.g. [22]). The transfer functions $T(k, z_{\mathrm{p}}, z_{\mathrm{rec}})$ in Poissonian gauge were calculated by the CLASS code [23]. They contain all relevant physics at linear order.

The peculiar gravitational potential $\varphi(k, \eta)$ in the radiation epoch (implying $w^{(\gamma)} \approx 1/3$) evolves as (see, e.g. [14])

$$\varphi(k, \eta) = \frac{3\, j_1(x)}{x}\varphi_0(k) \tag{13}$$

in Fourier space with initial conditions φ_0 at redshift $z = 10^7$, j_1 is the spherical Bessel function of first order and

$$x = \frac{k\,\eta}{\sqrt{3}}. \tag{14}$$

Furthermore, the linearised Einstein equations relate the total energy perturbations to the potential by

$$\delta_{\mathrm{tot}} = \frac{2}{3\mathcal{H}^2}\left(\Delta\varphi - 3\mathcal{H}\left[\varphi' + \mathcal{H}\varphi\right]\right). \tag{15}$$

With this equation we can calculate the initial φ_0 in Fourier representation as

$$\varphi_0(k) = \frac{3\,\mathcal{H}^2}{2k^2\,\frac{j_1(x)}{x} - 6\mathcal{H}\left[\frac{\partial}{\partial\eta}\left(\frac{j_1(x)}{x}\right) + \mathcal{H}\frac{j_1(x)}{x}\right]}\,\delta_{\mathrm{tot}}. \tag{16}$$

From there on we can use equation (13) again to calculate the potential and its derivatives at any time up to z_{eq}. The potential φ will tend to a constant after radiation-matter equality, as pressure becomes negligible. This means that the first and third term in equation (8) do not contribute to magnetogenesis from the epoch of radiation-matter equality to recombination.

[11] For further comments on the data see section 3 and [21].

We therefore evaluate these terms at radiation matter equality ($z \approx 3371$). From there on, these magnetic field terms are then propagated to recombination at redshift $z = 1088$ via the induction equation of magneto-hydrodynamics (MHD) (assuming again perfect conductivity):

$$\frac{\partial B}{\partial \eta} = \nabla \times (v \times B). \tag{17}$$

The fluid velocity v is also calculated in first order perturbation theory. The second term of equation (8) contains no time derivative of the potential and is therefore evaluated at recombination ($z = 1088$).

We illustrate the steps of the calculation in figure 1.

2.3. Simplifications

This calculation contains simplifying assumptions to keep the evolution equation for the magnetic field anaytically solvable. For completeness, those shall be discussed here.

The evolution of the potential via equation (13) is performed for a radiation dominated Universe with equation of state (3). The transition to the matter dominated era is modelled in an abrupt way with $w = \frac{1}{3}$ before equality and $w = 0$ afterwards. As the real transition is smooth, scales in the order of the equality horizon maybe affected by the modelling and magnetogenesis may even take place even after recombination. A heuristic modelling via e.g. hyperbolic functions was not performed as the additional time dependence makes the evolution equations for the potential not analytically solvable. This could be incorporated in the model if needed for the price of more contrieved calculations. Related to that, the coupling between electrons and photons is modelled via the tight coupling approximation as mentioned earlier. Thomson scattering is very efficient for scales larger than the mean free path of the photons, which at recombination can be estimated via

$$d_{\text{Thomson}} = \frac{1}{n_e a \sigma_T} \approx 2\ \text{Mpc}\,\text{h}^{-1} \tag{18}$$

in comoving scales. As we will see in the next section, our calculation is performed on a $\approx$ 1.3Mpc h^{-1} grid. Therefore the tight coupling should ideally be expanded to higher order in case of the Thomson coupling.

The above mentioned shortcomings where overcome by more detailed studies on the the generation of primordial magnetic fields via the Harrison mechanism, which have been conducted by several authors in the past 15 years. Gopal *et al* [24] showed that differences between electron and photon velocities lead to source terms for magnetic field generation. Saga *et al* [25] and Fenu *et al* [18] have refined this calculation by including anisotropic stresses stemming from the imperfect Thomson coupling. A similar calculation was done by Christopherson *et al* [26] first on the generation of vorticity in second order and later on the subsequent magnetic field generation [27] via the introduction of non-adiabatic pressure terms.

All of these approaches give source terms on which the Harrison mechanism can operate. The corresponding equations can in principle all be solved given suitable initial conditions. Only the approach shown above, however, gives an analytically integrable expression. All other models require the iterative solution of the respective magnetic field evolution equation in combination with all relevant quantities throughout the whole plasma era of the Universe up until recombination. This requires considerable computational effort to be implemented on the 512^3 voxel grid used in this work. For this reason, and as the field strengths

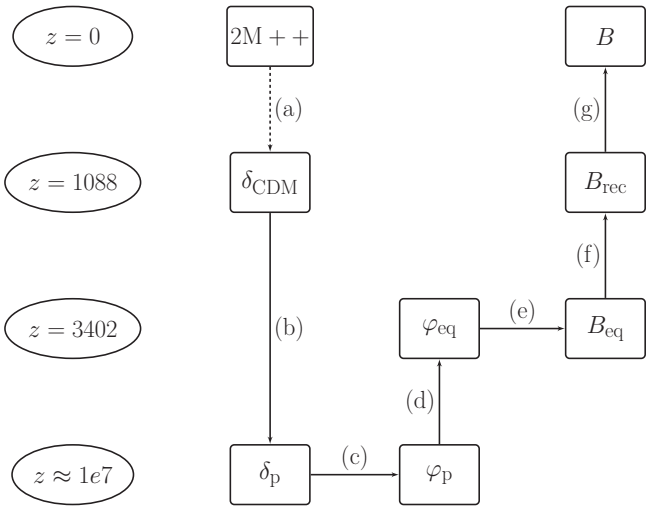

Figure 1. An illustration of the implemented algorithm. The ellipses indicate relevant redshifts. The labels near the arrows refer to the following steps: (a) dark matter inference from galaxy data via BORG, (b) linear dark matter transfer functions (equation (12)), (c) translation of dark matter density to potential φ (equation (16)), (d) time evolution of the potential via equation (13), (e) calculation of the magnetic field (equation (8)), (f) induction equation (equation (17)), (g) full MHD solver (see section 4).

which were found in [18, 24, 25, 27, 28] are comparable to the ones found by Mataresse [14], we find the above mentioned simplifications acceptable. Fidler *et al* [28] show that the exact treatment of the Thomson coupling gives rise to significant magnetogenesis even after last scattering, which highlights that a better modelling around recombination would be desirable, given that one can shoulder the resulting computational complications.

3. Data

This work builds upon three dimensional dark matter density fields previously inferred from the 2M++ galaxy compilation [29] via the BORG algorithm [30]. The BORG algorithm is a full scale Bayesian inference framework aiming at the analysis of the linear and mildly-non-linear regime of the cosmic large scale structure (LSS) [21, 31]. In particular it performs dynamical LSS inference from galaxy redshift surveys employing a second order Lagrangian perturbation model. As such the BORG algorithm naturally accounts for the filamentary structure of the cosmic web typically associated to higher order statistics as induced by non-linear gravitational structure formation processes. A particular feature, relevant to this work, is the ability of the BORG algorithm to infer Lagrangian initial conditions from present observations of the galaxy distribution [21, 30, 31]. More specifically the algorithm explores a LSS posterior distribution consisting of a Gaussian prior for the initial density field at a initial scale factor of $a = 0.001$ linked to a Poissonian likelihood model of galaxy formation at redshift z = 0 via a second order Lagrangian perturbation theory (2LPT) model (for details see [21, 30, 31]), that is conditioned to the 2M++ galaxy compilation [30]. Besides typical observational systematics and uncertainties, such as survey geometries, selection functions and noise this algorithm further accounts for luminosity dependent galaxy bias and performs automatic noise calibration [30]. The BORG algorithm accounts for all joint and correlated uncertainties in

inferred quantities by performing a Markov Monte Carlo chain in multi-million dimensional parameter spaces via an efficient implementation of a Hamiltonian Monte Carlo sampler [31]. As a result the algorithm provides a numerical representation of the LSS posterior in the form of data constrained realizations of the present three dimensional dark matter distribution and corresponding initial conditions from which it formed. It is important to remark that each individual Markov sample qualifies for a plausible realisation of the LSS. Each sample of the dark matter distribution consists of a box with 256^3 grid points and 677.7 Mpc h^{-1} edge length, resulting in a resolution of approximately 2.5 Mpc h^{-1}. For one sample of BORG we increase the resolution of the grid to 512^3 by augmenting the large scale modes with random fluctuations consistent with the known dark matter power spectrum. This sample is then propagated into todays configuration via a MHD simulation as explained in the following section. As described above we now apply the Harrison mechanism on data constrained initial conditions of the Nearby Universe.

4. MHD simulations

The MHD computation is started from the magnetic field generated at $z = 1088$ and is evolved to $z = 0$ using the cosmological code ENZO [32]. ENZO is a grid based code that follows the dynamics of dark matter with a particle-mesh N-body method, and a combination of several possible shock-capturing Riemann solvers to evolve the gas component [32]. The MHD method employed in this paper is the Dedner 'cleaning' method [33], which makes use of hyperbolic divergence cleaning to keep the (spurious) divergence of the magnetic field as low as possible during the computation. The magnetic fluxes across the cells are computed with a piecewise linear interpolation method and the fluxes are combined with a Lax-Friedrichs Riemann solver, with a time integration based on the total variation diminishing second order Runge–Kutta scheme [34]. Thanks to the capabilities of ENZO of selectively refining interesting patches in the domain at higher resolution, we used adaptive mesh refinement (AMR) to selectively increase the dynamical resolution in the formation region of galaxy clusters and groups, which is necessary to properly resolve structure formation and overcome the effect of magnetic field dissipation in converging flows at low resolution [35].

In detail, we apply AMR only in the innermost $(120\ \mathrm{Mpc}\ h^{-1})^3$ region of the simulation, centred on the Milky Way location, and allowed for 5 levels of refinement (by increasing the resolution of a factor 2 at each level, therefore up to a $2^5 = 32$ refinement) whenever the local gas/dark matter density exceeded the mean density of surrounding cells by a factor of 3; the procedure is recursively repeated at each AMR level. This ensures that the magnetic field evolution in the innermost clusters regions is typically followed with a spatial resolution of 61–122 kpc h^{-1} (comoving) within the innermost AMR region of our volume. To confirm the consistency of our result, we show a slice through the gas density resulting from the simulation in figure 2. This plot indicates that we reproduce the large scale structure consistently with observations.

5. Reconstructing primordial magnetic fields

We will present the results of our work in two steps. First we focus on the statistical properties of the field at recombination. By applying the procedure described in the previous sections to an ensemble of data constrained initial conditions we can propagate observational uncertainties of the matter distribution as traced by the 2M++ survey to the derived magnetic fields. In doing so we arrive at an ensemble of initial magnetic fields which constitutes a numerical

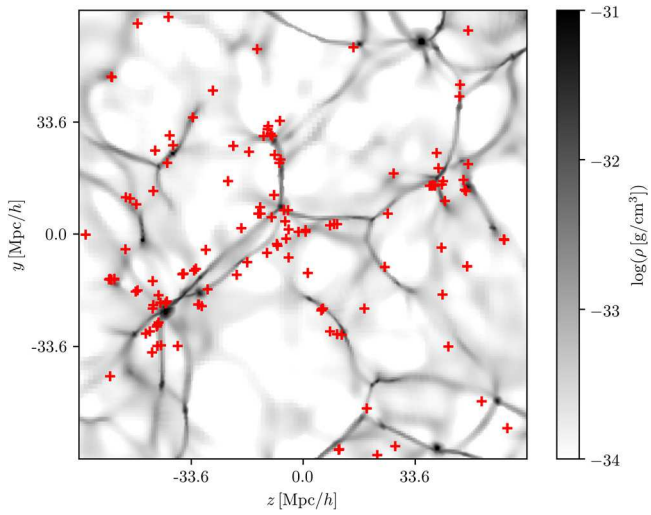

Figure 2. A slice through the gas density distribution of the innermost region of the box averaged over 6 voxels in x direction at redshift $z = 0$ as a result of the ENZO simulation. The plane is about 1 Mpc h^{-1} thick. The red crosses indicate the positions of galaxies found by the 2M++ survey in the same volume.

description of the magnetic field posterior distribution at redshift $z = 1088$ conditional on 2M++ galaxy data. The goal here is to show how these uncertainties translate onto the calculated primordial magnetic field and to give scale dependent estimates on correlations and field strengths at this epoch.

The second part will show the results after the MHD run at redshift $z = 0$. Here we will also turn our face on one particular realisation of the primordial magnetic field. We will show the large scale primordial magnetic field of some clusters of galaxies as well as the field in the close proximity to Earth. The resulting fields are available for download at[12].

5.1. Recombination

5.1.1. Means and Variances. To illustrate the uncertainties we show slice plots of the input data and the resulting magnetic field strength at recombination in figures 3 and 4. All plots are slices through the $(677.7\ \mathrm{Mpc}\ h^{-1})^3$ cube. The first plot shows the field resulting form one particular sample of the BORG algorithm. The comoving root mean square (rms) field strength is around 10^{-23} G. The uncertainties are rather large compared to the mean. This is a consequence of he sparse data, which rather constrains the large scales than the small ones. Structures in the field appear to be rather small, typically with Mpc-scale (see section 5.1.2).

Figures 3 and 4 give an impression of the Bayesian properties of the BORG algorithm, which is translated onto our magnetic field realisations. They show the posterior mean and variance field of the magnetic field strength generated from 351 samples from the BORG posterior distributions. Areas which are highly constrained by data have well distinguishable structures in the mean, and have low uncertainty variance. The outer regions are less constrained, structures which are well visible in one particular sample are averaged out in the mean, and the variance is high.

[12] https://wwwmpa.mpa-garching.mpg.de/∼ensslin/research/data/data.html or https://doi.org/10.5281/zenodo.1190925

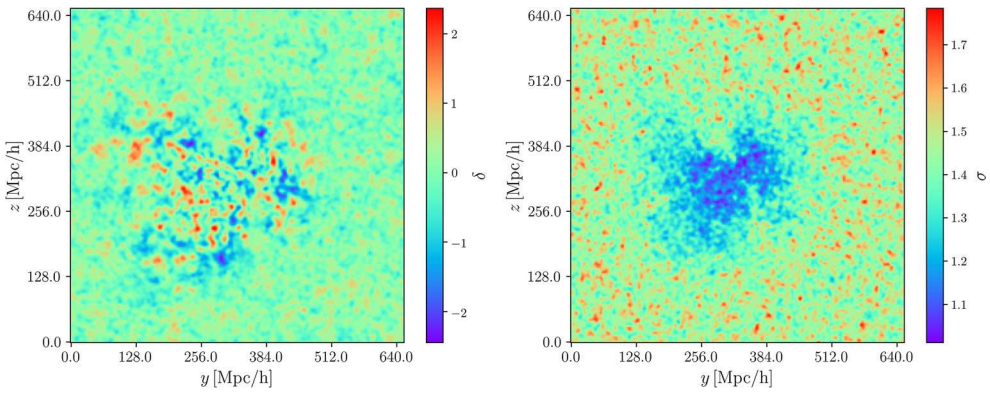

Figure 3. The posterior mean (left) and uncertainty standard deviation field of the dark matter overdensities (right) at redshift $z = 1000$. This is the mean of the input data for our calculation averaged over 351 posterior samples of the matter field as generated by BORG. Our galaxy is centered in the middle. Areas close to the center a very pronounced in the mean, while areas further away are blurred out during the averaging. This reflects the Bayesian nature of the BORG algorithm, as the closer areas are very constrained by data, which leads to a relatively narrow posterior distribution in each pixel as reflected by the uncertainty variance. Therefore each sample looks similar there. The outer regions are barely constrained by data, leading to high uncertainties in the posterior.

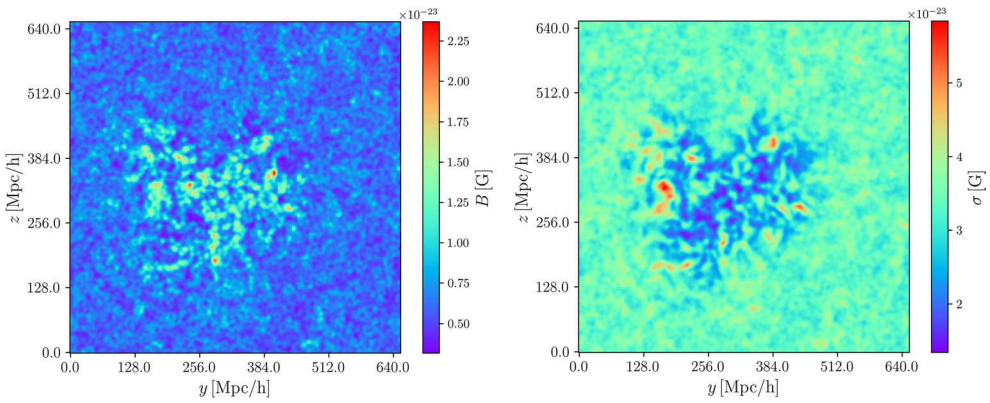

Figure 4. The posterior mean (left) and uncertainty standard deviation (right) field of the absolute value of the Harrison magnetic field at redshift $z = 1088$. Just as in the case of the initial data in figure 3, we note a very similar pattern in the mean and variance plots for regions closer and further away from Earth. The uncertainties of the density fields translate into uncertainties of the magnetic field.

5.1.2. Power spectra. Information on the correlation structure of a scalar field $s(x)$ can be gained from the corresponding scalar power spectrum defined as:

$$\langle s(k) s^*(k') \rangle_{P(s)} = (2\pi)^3 \, \delta(k - k') \, P_s(k) \tag{19}$$

where the asterisk denotes the complex conjugate. In case of a magnetic field B, the statistically isotropic and homogeneous correlation tensor is defined as

$$\langle B_i(k) B_j^*(k') \rangle_{P(B)} = (2\pi)^3 \, \delta(k - k') \, M_{ij}(k), \tag{20}$$

where the tensor M_{ij} is defined as (see e.g. [19]):

$$M_{ij} = \frac{1}{2}\left(\delta_{ij} - \hat{k}_i\hat{k}_j\right) P_{\mathrm{B}}(k) + i\epsilon_{ijk}\hat{k}_k P_{\mathrm{H}}(k). \tag{21}$$

The helical part $P_{\mathrm{H}}(k)$ is assumed to be zero in this work. The magnetic field power spectra are therefore just the trace component of the magnetic field power spectrum tensor.

As a consistency check we first show the power spectrum of the initial CDM field and the scalar perturbations φ through some of the time steps of the algorithm in figures 5–7. These plots show the averaged spectra from 351 samples from BORG together with the corresponding uncertainties. We also show the magnetic field power power spectrum in figure 8.

Despite some deviations on very large scales reflecting the uncertainties mentioned in the previous section, the spectra agree to a very good level with our expectations. These deviations can be noted in our intitial matter fields coming from the BORG algorithm (figure 5) and further on in all the other averaged power spectra. We note a clear k^{-3} dependence in the primordial potential and matter power spectrum corresponding to an approximately unity spectral index as expected for uncorrelated and scale invariant structures [36, 37]. We can compare the spectrum with the Planck results as a consistency check, see table 2 and the dashed line in figure 6.

The potential power spectrum at matter-radiation equality drops shortly above $k = 0.1\,\mathrm{Mpc}^{-1}\,\mathrm{h}$, indicating the size of the horizon at that time. At small scales, the spectrum shows oscillations in Fourier space, which stem from the functional form of the potential evolution equation in equation (13). Physically speaking, these are the Baryon-accoustic oscillations (BAO's) induced by horizon crossing during the radiation epoch. The uncertainties again agree with the initial dark matter spectrum. The resulting power spectrum of the magnetic field is plotted in figure 8. It rises for small k-values with approximately $k^{3.5}$ as expected from our discussion in section 2 and peaks at $k_{\mathrm{peak}} \approx 2 \cdot 10^{-1}\,\mathrm{Mpc}^{-1}\,\mathrm{h}$. The plot shows little 'bumps' on small scales, which are remnants of the oscillating potential in the radiation epoch. At this point it shall also be noted that in the time frame of our calculation any turbulence due to primordial velocity perturbations is not relevant. In [39] the authors show that given these perturbations the very Early Universe has Reynolds numbers in the range of 10^3. This then gives the perfect framework for a small-scale dynamo to amplify the magnetic seed fields originating from the Harrison effect to fields with strengths of approximately 10^{-15} G, but with typical correlation lengths of the order of parsecs. Given the Mpc resolution of our grid, this is not relevant for this work.

5.1.3. Scale dependent mean field. To give a more intuitive picture of the expected magnetic field strengths, we convolve the magnetic field power spectrum with a Gaussian kernel in position space to get an estimate for B given a scale of reference λ.

$$B_\lambda^2 = \frac{1}{(2\pi)^3}\int P_B(k)\, e^{-\frac{k^2\lambda^2}{2}}\, \mathrm{d}^3k. \tag{22}$$

The result of this operation is shown in figure 9. For scales reaching from 2.65 Mpc h^{-1} to $\approx$ 10 Mpc h^{-1} the magnetic field strength weakly declines and has a typical strength of approximately 10^{-23} G. For scales larger than 10 Mpc h^{-1}, B_λ roughly scales as

$$B_\lambda \sim \lambda^{-2.5}. \tag{23}$$

The field strength reaches from 10^{-23} G at the smallest scales just over 1 Mpc h^{-1} to less than 10^{-27} G at scales over a 100 Mpc h^{-1}. This information is of course closely related to the magnetic field power spectrum.

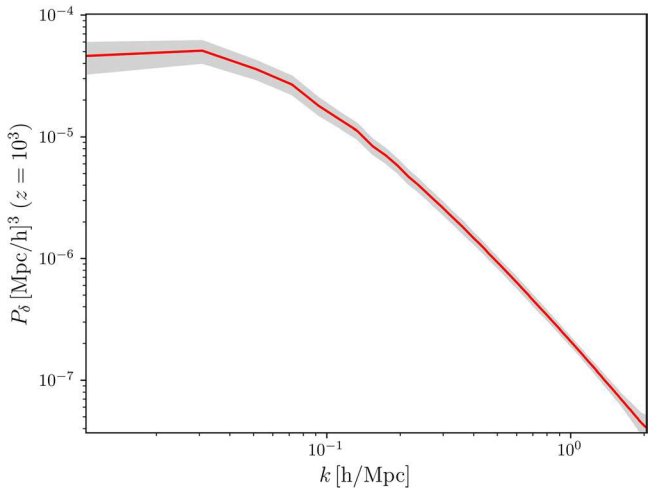

Figure 5. The matter power spectrum at $z = 10^3$. This is the spectrum of the input data. The red line is the mean averaged over the 351 samples. The grey area gives the uncertainty in the spectrum.

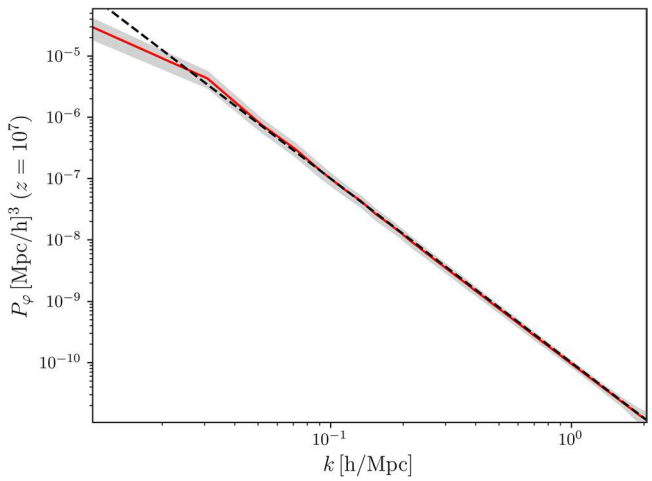

Figure 6. The power spectrum of the primordial scalar perturbations at redshift $z = 10^7$ as extracted from the cosmic structure reconstruction by [21]. The dashed black line indicates the scale invariant spectrum normalized with the Planck amplitude parameter $\mathcal{A}_s$, see table 2.

5.2. Today

5.2.1. Field strength and correlation structure. In figure 10 we depict the power spectrum of the magnetic field today for one sample of the BORG posterior. We show the complete spectrum as well as the void power spectrum inferred via negleting dens voxels with gas density $\rho > 3 \cdot \overline{\rho}$ and the critical filter technique [40], which assumes that the unmasked regions are typical for the whole volume. The BAO signature and most small structures have been destroyed during structure formation, leading to a mostly red spectrum. For the complete spectrum and the voids, most power still lies on scales of about $k_{\mathrm{peak}} \approx 10^{-1}\,\mathrm{Mpc}^{-1}\,\mathrm{h}$. The

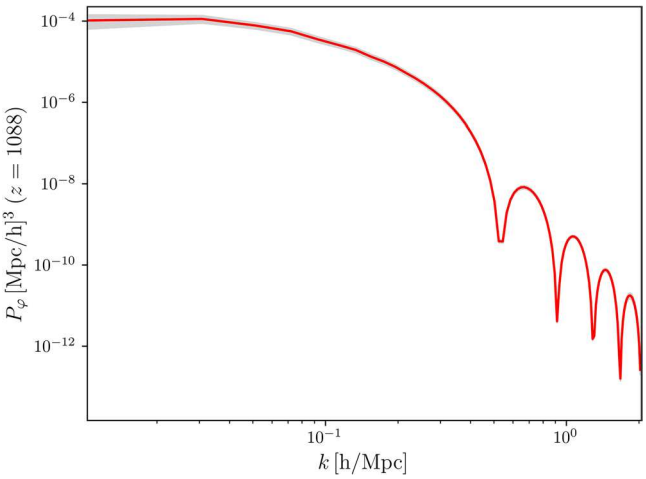

Figure 7. The power spectrum of the scalar perturbations at redshift $z = 3402$ at the end of the radiation dominated epoch. The oscillations in the spectrum are the Baryon-Accoustic Osclillations (BAO).

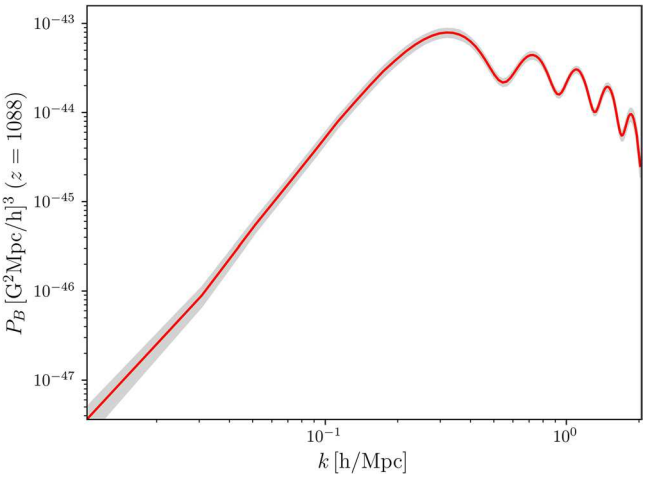

Figure 8. The power spectrum of the magnetic field at redshift $z = 1088$ just before recombination. The spectrum is defined of a vector field is defined in equations (20) and (21). The spectrum peaks at approximately $\approx 3 \cdot 10^{-1}$ Mpc^{-1} h.

Table 2. Comparison of inflation parameters provided by the Planck collaboration [38] and as inferred from the samples used in this work.

	Planck (2015)	This work
$\ln\left(10^{10}\mathcal{A}_s\right)$	3.064 ± 0.023	≈ 3.1
n_s	0.9667 ± 0.0040	≈ 1

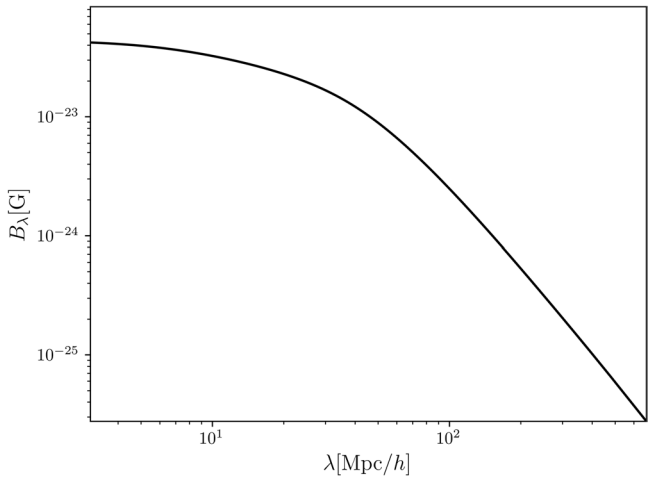

Figure 9. Scale averaged magnetic field at recombination. This is the result of equation (22).

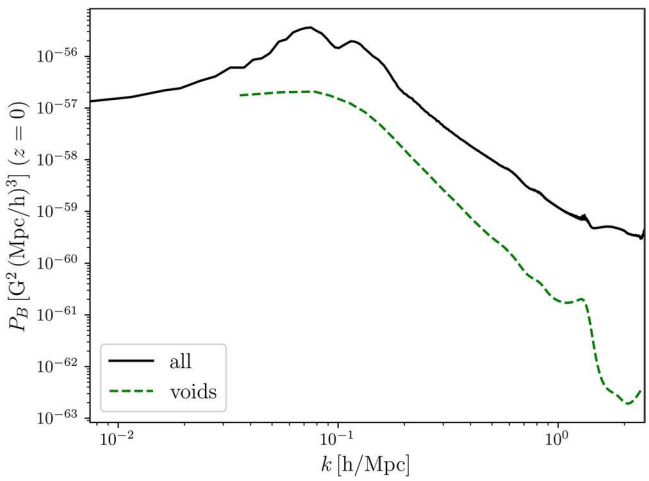

Figure 10. The magnetic power spectrum at $z = 0$, defined according to equation (20). The black line indicates the spectrum for the complete magnetic field in the box. The green dashed line indicates the void power spectrum, computed only from a part of the box. Here we considered voxels with gas density $\rho < 3 \cdot \overline{\rho}$ as void voxels. The void power spectrum was inferred using the critical filter technique [40], which assumes that the unmasked regions are typical for the whole volume.

morphology of the complete power spectrum is rather similar to the void power spectrum, which is expected, as they compromise the largest volume share of the Universe and calculating a power spectrum is effectively a volume averaging procedure. The decrease at large scales again reflects the solenoidality of magnetic fields ($\nabla \cdot B = 0$) for uncorrelated signals [19], as the large scale structure has a characteristic size and therefore larger scales are not strongly causally connected via gravity.

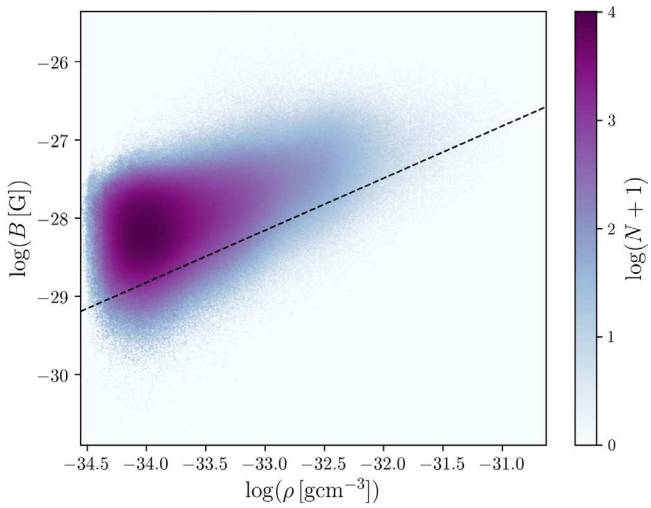

Figure 11. Joint histogram of the magnetic field and matter density at redshift $z = 0$ with 512^2 bins. The dashed line indicates the $B \propto \rho^{2/3}$ relation resulting from the flux freezing of the magnetic field lines. This relation is also observed in simulations starting with unconstrained magnetic field conditions, see e.g. [41].

In figure 11 we show the joint probability function of matter density and magnetic field strength. Most of the probability mass lies on rather small densities, with varying magnetic field strengths. Large densities tend to be associated with large magnetic field strength. The lower bound of this plot follows a $B \propto \rho^{\frac{2}{3}}$ proportionality, which was already found in previous simulations, e.g.: [41]. All in all this leads to the picture that the magnetic field in the low density areas which are relatively little affected by structure formation mostly retain their correlation structure and morphology. After recombination, the field is frozen into the plasma. Therefore the field strength scales with $a(t)^{-2}$, explaining the field strengths somewhere around 10^{-29} G. Within dense structures the field is at least amplified up to $10^{-26.5}$ G. We underline this view with specific examples in the next chapter.

5.2.2. Field realisations. In figures 12 and 13 we show structures in the magnetic field and the density field which belong to different morphological features of the Local Universe. We find that the magnetic field strength strongly correlates with the gas density in all of these structures, consistent with a frozen-in behaviour of magnetic fields. In very dense clusters such as Virgo and Perseus-Pisces in figure 12 the magnetic field morphology seems to be driven by the infall of matter on the cluster. Of course the simulation is too coarse to correctly cover the structure formation and magnetic field behaviour on small scales within these structures, for this reason any small scale structures in these plots are highly uncertain. Also the maximum magnetic field strength maybe higher, as we cannot resolve any potential dynamo mechanism during structure formation. Magnetic field amplification of a primordial seed field via turbulence and dynamos in clusters and galaxies is discussed in e.g. [42–45]. In underdense regions as depicted in the upper image in figure 13, we observe a morphology similar to the initial conditions, with a charcteristic scale of a few Mpc/h. Apart from the aforementioned $a(t)^{-2}$ dependence of the field strength, the morphology seems to relatively unaffected, which is consistent with our view of a 'frozen' magnetic field. In the lower image of figure 13 we

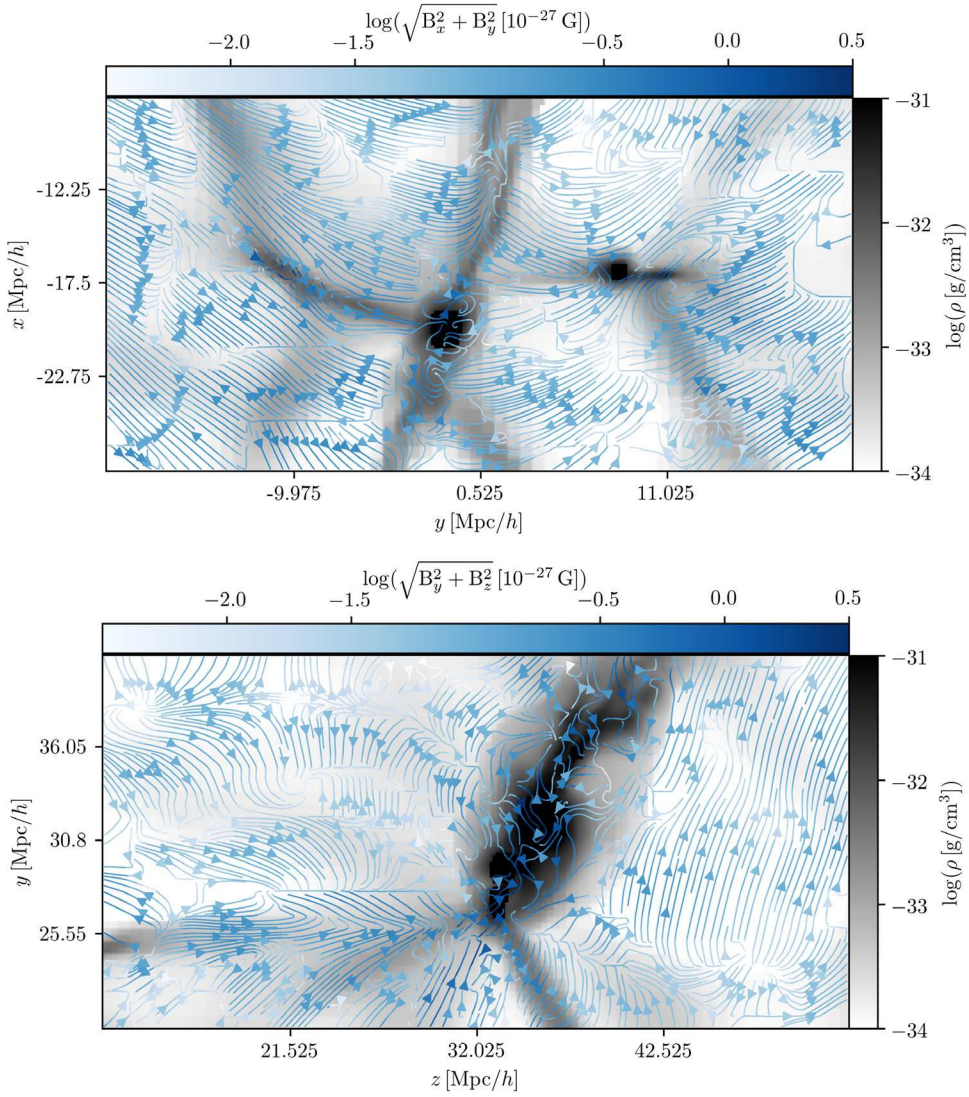

Figure 12. The magnetic field and gas matter density in a slice trough the Virgo (above) and the Perseus-Pisces (below) cluster. The plots shows the gas matter density overplotted with the $y - z$ components of the magnetic field vectors. All colorbars have a logarithmic scaling. The coordinates are defined via the equatorial plane with reference to the galactic centre. The choice of the slice is purely for artistic reasons.

show the magnetic field in a slice around our galaxy. The field here is slightly amplified up to field strengths of 10^{-28} G, as a slight overdense structure seems to have formed in the region, which may correspond to the Local Group. The Local Group has a typical scale of about 2 Mpc, which is slightly below the smallest data constraint scale in our calculation, making the association difficult.

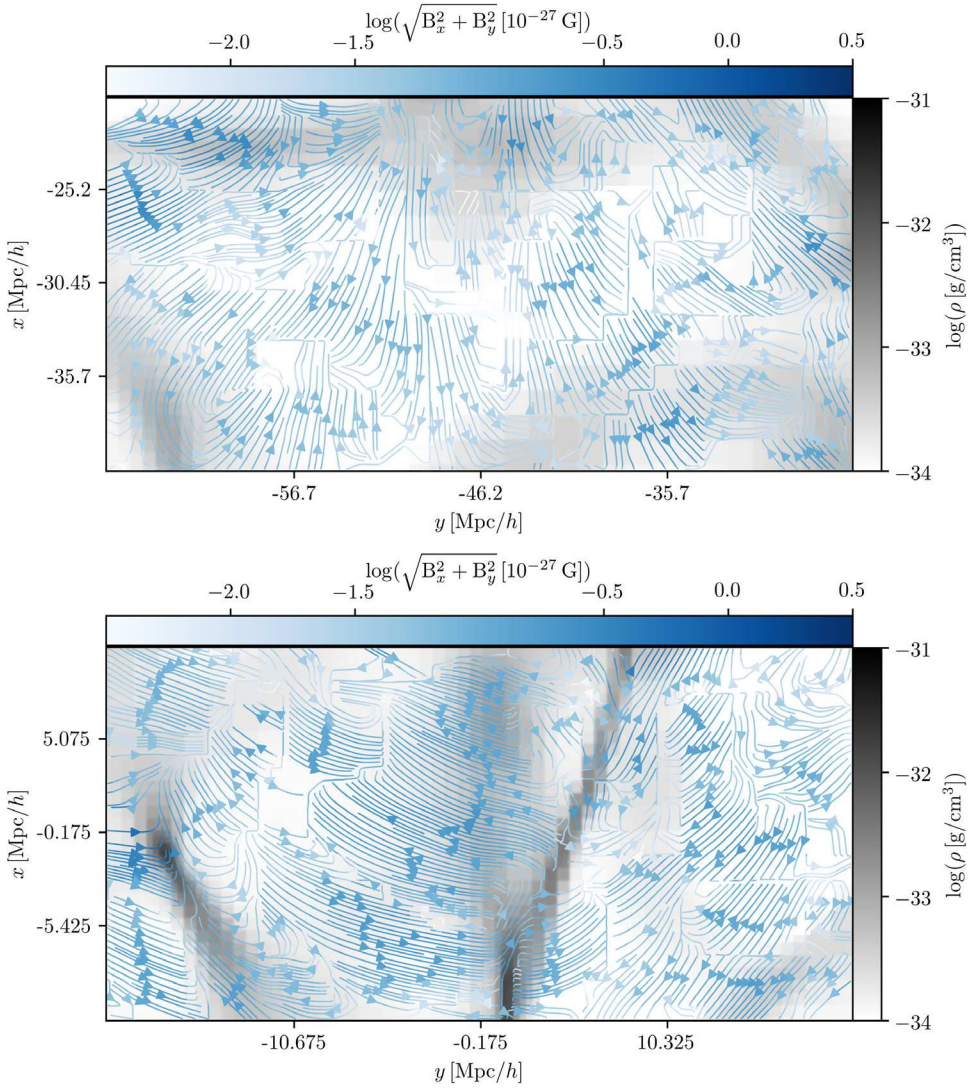

Figure 13. The magnetic field and gas matter density in an underdense region (above) and around the galactic center in the $x - y$ plane. The plots shows the gas matter density overplotted with the $x - y$ components of the magnetic field vectors. All colorbars have a logarithmic scaling. The coordinates are defined via the equatorial plane with reference to the galactic centre.

5.2.3. Full sky maps. We can use the results of the ENZO simulation to estimate the expected Faraday rotation of linear polarized light under the influence of a magnetic field. Faraday rotation measure (RM) is calculated via

$$\mathrm{RM} = \frac{e^3}{2\pi m_e^2 c^4} \int_0^{R_{\max}} n_{\mathrm{th}}\, B\, \mathrm{d}r \tag{24}$$

in cgs units (see e.g. [48]). It is essentially a line of sight (LOS) integration up to a distance $R_{\max}$ over the magnetic field B weighted with the electron number density n_{th}. This can be

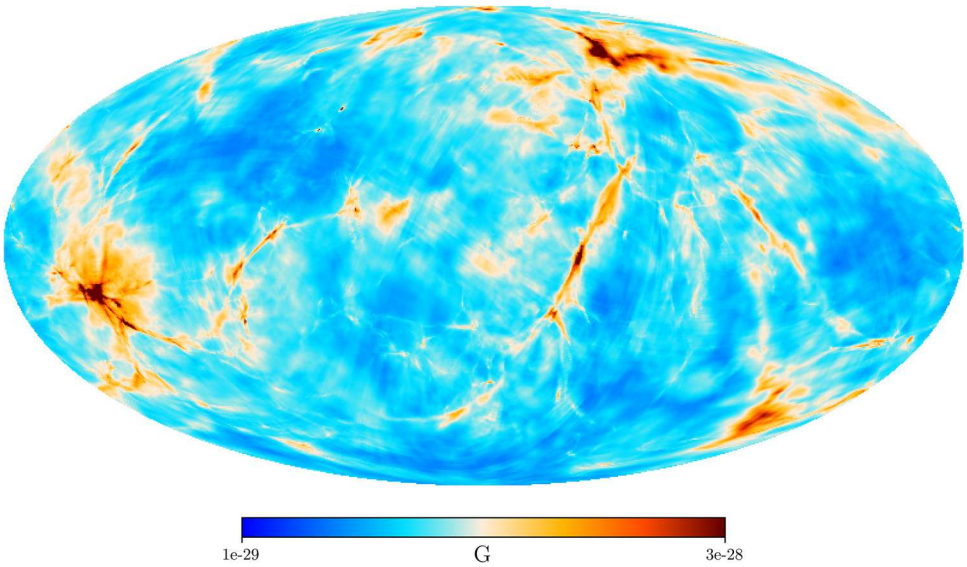

Figure 14. The magnetic field strength averaged over line of sights in units of Gauss for sources within a distance of 60 Mpc/h from Earth. The plot is in galactic coordinates. The two dominant clusters in this image are Persues Pisces in the middle left of the image and Virgo close to the North pole. Close ups of both structures are provided in figure 12.

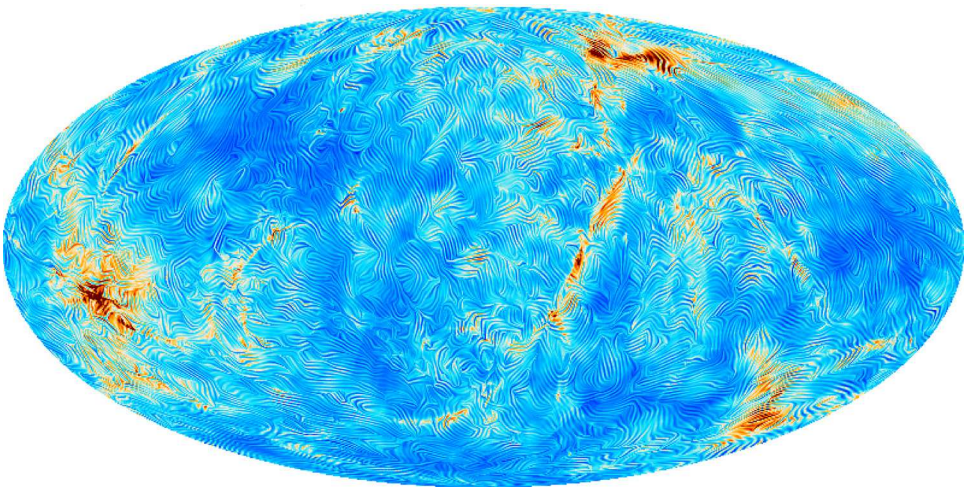

Figure 15. A polarization-like plot visualizing the magnetic field morphology perpendicular to the LOS. This plot was generated using the 'Alice' module of the HEALPix software[13] [46] and the linear integral convolution algorithm [47]. The plot is in galactic coordinates.

[13] http://healpix.sourceforge.net

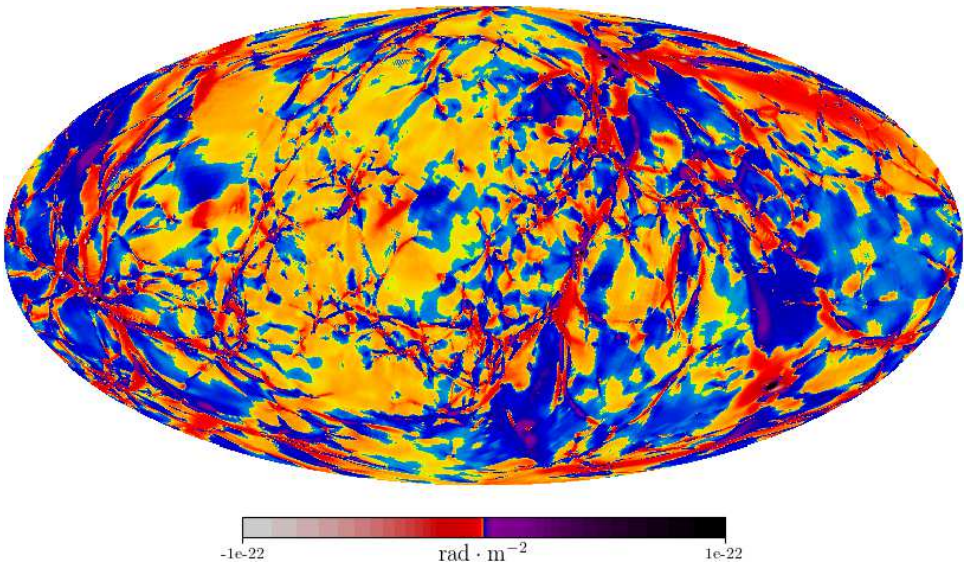

Figure 16. The primordial magnetic field Faraday rotation measure for polarized sources located within a distance of 60 Mpch^{-1} from earth in units of radians per square metre. The plot is in galactic coordinates. The colormap is logarithmic on both the negative and the positve regime with a linear scaling between -10^{-29} and 10^{-29} rad·m^{-2}, connecting both parts of the scale. We used the rescaled gas mass density as an estimate for the electron number density.

computed using the publicly available Hammurabi Software [49], which performs the necessary LOS integration over a sphere around the Earth[14]. The result can be seen in figure 16. The same software is also able to calculate the dispersion measure of electrons (DM) and the LOS averaged absolute magnetic field strength,

$$\mathrm{DM} = \int_0^{R_{\max}} n_{\mathrm{th}}\, \mathrm{d}r, \tag{25}$$

shown in figures 17 and 14. These maps nicely trace dense structures in the sphere over which we integrated. We also used the output of Hammurabi for the LOS perpendicular components of the magnetic to generate a polarization like plot in figure 15, which traces the magnetic field morphology in the sphere. Comparing the plots we see that areas of large RM correspond to large electron densities, as we expect given the linear n_{th} dependence of RM. We also note again that the magnetic field strength and morphology correlates with the density.

Of course the expected signal is beyond any chance of measurability, and in the realistic case we expect that the memory of any such tiny seed field within clusters is entirely lost due to the dynamo amplification process [50], which is expected to be much more efficient on scales smaller than what is resolved at our resolution here. The void signal, however, although a few order of magnitudes smaller, may be relatively undisturbed by such processes, at least away from other possible sources of magnetisation, like dwarf galaxies [51].

[14] We used a reimplementation of Hammurabi (Wang *et al*, in prep.); https://bitbucket.org/hammurabicode/hamx

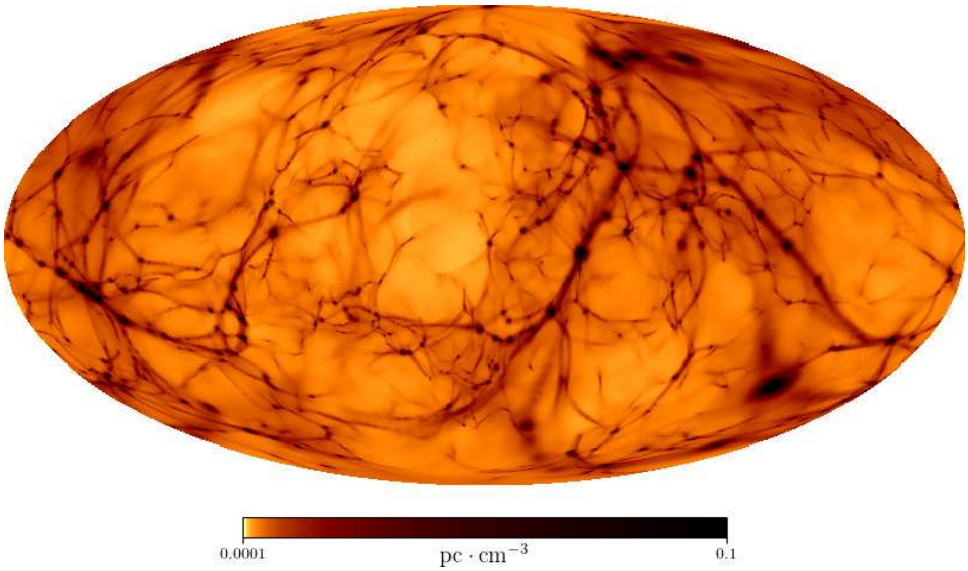

Figure 17. The electron dispersion measure in units of parsecs per cubic centimetre for sources within a distance of 60 Mpc/*h* from Earth. The plot is in galactic coordinates. We used the rescaled gas mass density as an estimate for the electron number density. The two dominant clusters in this image are Persues Pisces in the middle left of the image and Virgo close to the North pole. Close ups of both structures are provided in figure 12.

6. Summary and discussion

We calculated the large scale primordial magnetic field originating from the Harrison effect [15] and second order vorticity generation in the radiation dominated era. This is the first time a data constraint reconstruction of the remnant of a primordial magnetic field was achieved.

For that, we used our knowledge about the large scale structure in the Universe coming from the 2M++ galaxy survey and the BORG algorithm to infer the corresponding density distributions deep in the radiation epoch. Using an existing formalism for the magnetic field generation from these initial conditions, we then found at recombination a field coherent on comoving scales in the 10 Mpc h^{-1} regime, with a maximum field strength of about 10^{-23} G at these scales. By means of a MHD simulation we evolved the magnetic field through structure formation and came up with field strengths higher than $\approx 10^{-27}$ G and $\approx 10^{-29}$ G in clusters of galaxies and voids, respectively. We specifically showed the structure of the field around well known structures in the Local Universe, such as the Virgo and Perseus Pisces cluster.

The above results, including the statistical properties of the magnetic fields, the morphology of the field on above Mpc scales and the expected observables shown in figures 16 and 17 rely only on the assumption of a ΛCDM cosmology and conventional plasma physics. We introduced further simplifications such as the tight coupling approximation and the simplified modelling around the radiation matter equality due to computational constraints. In [18, 25], the authors calculated the correct evolution equations without these simplifications, leading to slightly different spectra, but comparable magnetic field strengths. Large scale magnetic fields can also be produced by more speculative mechanisms for primordial magnetogenesis, by transferring magnetic energy of small scaled magnetic fields to larger scales via an inverse cascade and by magnetogenesis driven by radiation pressure during reionisation [52]. For this reason, we

view our results as a lower limit on the magnetic field strength in the Local Universe. This is especially true for clusters, as for once small scales are not strongly constraint by our data and moreover we where not able to resolve the relevant scales for magnetic field amplification via turbulence, as predicted by e.g. Subramanian *et al* [53]. We did arrive at magnetic field strengths which could act as a seed field for the galactic dynamo [54], however given the fact that we cannot adequately resolve sub-Mpc scales and galactic magnetic fields maybe explained without a primordial seed, we refrain from giving an estimate to which extent the Harrison magnetic field could have influenced galactic magnetic fields. A possible explanation for the non-observation of TeV-photons from blazars are void magnetic fields of strength 10^{-15} G [1, 12], among other explanations [5]. If these fields exist, our prediction is not sufficient to explain them.

Considering the rather conservative assumptions made in our calculations, we can provide a credible lower bound on the strength of the large scale magnetic field today and an impression of its expected morphology. The logical next step building up on this work would be a refinement of the calculation via the implementation of more sophisticated formalisms for the generation of primordial magnetic fields, especially including a more accurate baryon photon interaction treatment.

Acknowledgments

We thank four anonymous referees for insightful comments. This research was supported by the DFG Forschungsgruppe 1254 'Magnetisation of Interstellar and Intergalactic Media: The Prospects of Low-Frequency Radio Observations' and the DFG cluster of excellence 'Origin and Structure of the Universe' (www.universe-cluster.de). This work made in the ILP LABEX (under reference ANR-10-LABX-63) was supported by French state funds managed by the ANR within the Investissements dAvenir programme under reference ANR-11-IDEX-0004-02. GL is supported in part by the French ANR BIG4, grant ANR-16-CE23-0002. The cosmological simulations described in this work were performed using the ENZO code (http://enzo-project.org), which is the product of a collaborative effort of scientists at many universities and national laboratories. We gratefully acknowledge the ENZO development group for providing extremely helpful and well-maintained online documentation and tutorials. The computation presented in this work was produced on at Jülich Supercomputing Centre (JSC), under projects no. 10755 and 11764. FV acknowledges financial support from the European Union's Horizon 2020 research and innovation programme under the Marie-Sklodowska-Curie grant agreement no.664931, and from the ERC Starting Grant 'MAGCOW', no.714196. DP acknowledges financial support by the ASI/INAF Agreement I/072/09/0 for the Planck LFI Activity of Phase E2 and by ASI Grant 2016-24-H.0. Some of the results in this paper have been derived using the HEALPix [46] package.

ORCID iDs

Sebastian Hutschenreuter https://orcid.org/0000-0002-6952-9688
Franco Vazza https://orcid.org/0000-0002-2821-7928

References

[1] Neronov A and Vovk I 2010 Evidence for strong extragalactic magnetic fields from Fermi observations of TeV blazars *Science* **328** 73–5

[2] Neronov A and Semikoz D V 2009 Sensitivity of γ-ray telescopes for detection of magnetic fields in the intergalactic medium *Phys. Rev.* D **80** 123012
[3] Tavecchio F, Ghisellini G, Foschini L, Bonnoli G, Ghirlanda G and Coppi P 2010 The intergalactic magnetic field constrained by Fermi/large area telescope observations of the TeV blazar 1ES0229+200 *Mon. Not. R. Astron. Soc.* **406** L70–4
[4] Dolag K, Kachelriess M, Ostapchenko S and Tomas R 2010 Lower limit on the strength and filling factor of extragalactic magnetic fields *ApJL* **727** L4
[5] Pfrommer C, Broderick A E, Chang P, Puchwein E and Springel V 2013 The physics and cosmology of TeV blazars in a nutshell (arXiv e-prints)
[6] Saveliev A, Jedamzik K and Sigl G 2012 Time evolution of the large-scale tail of nonhelical primordial magnetic fields with back-reaction of the turbulent medium *Phys. Rev.* D **86** 103010
[7] Saveliev A, Jedamzik K and Sigl G 2013 Evolution of helical cosmic magnetic fields as predicted by magnetohydrodynamic closure theory *Phys. Rev.* D **87** 123001
[8] Brandenburg A, Kahniashvili T and Tevzadze A G 2015 Nonhelical inverse transfer of a decaying turbulent magnetic field *Phys. Rev. Lett.* **114** 075001
[9] Reppin J and Banerjee R 2017 Nonhelical turbulence and the inverse transfer of energy: a parameter study *Phys. Rev.* E **96** 053105
[10] Kandus A, Kunze K E and Tsagas C G 2011 Primordial magnetogenesis *Phys. Rep.* **505** 1–58
[11] Subramanian K 2016 The origin, evolution and signatures of primordial magnetic fields *Rep. Prog. Phys.* **79** 076901
[12] Yamazaki D G, Kajino T, Mathews G J and Ichiki K 2012 The search for a primordial magnetic field *Phys. Rep.* **517** 141–67
[13] Durrer R and Neronov A 2013 Cosmological magnetic fields: their generation, evolution and observation *Astron. Astrophys. Rev.* **21** 62
[14] Matarrese S, Mollerach S, Notari A and Riotto A 2004 Large-scale magnetic fields from density perturbations *Phys. Rev.* D **71** 043502
[15] Harrison E R 1970 Generation of magnetic fields in the radiation era *Mon. Not. R. Astron. Soc.* **147** 279
[16] Dorn S 2016 Bayesian inference of early-universe signals *Dissertation* (http://nbn-resolving.de/urn:nbn:de:bvb:19-191317)
[17] Ade P A R *et al* (Planck Collaboration) 2016 Planck 2015 results. XIII. Cosmological parameters *Astron. Astrophys.* **594** A13
[18] Fenu E, Pitrou C and Maartens R 2011 The seed magnetic field generated during recombination *Mon. Not. R. Astron. Soc.* **414** 2354–66
[19] Durrer R and Caprini C 2003 Primordial magnetic fields and causality *J. Cosmol. Astropart. Phys.* JCAP11(2003)010
[20] Turner M S and Widrow L M 1988 Inflation-produced, large-scale magnetic fields *Phys. Rev.* D **37** 2743–54
[21] Jasche J, Leclercq F and Wandelt B D 2015 Past and present cosmic structure in the SDSS DR7 main sample *J. Cosmol. Astropart. Phys.* JCAP1(2015)036
[22] Ma C-P and Bertschinger E 1995 Cosmological perturbation theory in the synchronous and conformal newtonian gauges *Astrophys. J.* **455** 7
[23] Blas D, Lesgourgues J and Tram T 2011 The cosmic linear anisotropy solving system (CLASS). II: Approximation schemes *J. Cosmol. Astropart. Phys.* JCAP07(2011)034
[24] Gopal R and Sethi S K 2005 Generation of magnetic field in the pre-recombination era *Mon. Not. R. Astron. Soc.* **363** 521–8
[25] Saga S, Ichiki K, Takahashi K and Sugiyama N 2015 Magnetic field spectrum at cosmological recombination revisited *Phys. Rev.* D **91** 123510
[26] Christopherson A J, Malik K A and Matravers D R 2011 Estimating the amount of vorticity generated by cosmological perturbations in the early universe *Phys. Rev.* D **83** 123512
[27] Nalson E, Christopherson A J and Malik K A 2014 Effects of non-linearities on magnetic field generation *J. Cosmol. Astropart. Phys.* JCAP9(2014)023
[28] Fidler C, Pettinari G and Pitrou C 2016 Precise numerical estimation of the magnetic field generated around recombination *Phys. Rev.* D **93** 103536
[29] Lavaux G and Hudson M J 2011 The 2M++ galaxy redshift catalogue *Mon. Not. R. Astron. Soc.* **416** 2840–56
[30] Lavaux G and Jasche J 2016 Unmasking the masked Universe: the 2M++ catalogue through Bayesian eyes *Mon. Not. R. Astron. Soc.* **455** 3169–79

[31] Jasche J and Wandelt B D 2013 Bayesian physical reconstruction of initial conditions from large-scale structure surveys *Mon. Not. R. Astron. Soc.* **432** 894–913
[32] Bryan G L *et al* (Enzo Collaboration) 2014 Enzo: an adaptive mesh refinement code for astrophysics *ApJS* **211** 19
[33] Dedner A, Kemm F, Kröner D, Munz C-D, Schnitzer T and Wesenberg M 2002 Hyperbolic divergence cleaning for the MHD equations *J. Comput. Phys.* **175** 645–73
[34] Wang P and Abel T 2009 Magnetohydrodynamic simulations of disk galaxy formation: the magnetization of the cold and warm medium *Astrophys. J.* **696** 96–109
[35] Vazza F, Brüggen M, Gheller C and Wang P 2014 On the amplification of magnetic fields in cosmic filaments and galaxy clusters *Mon. Not. R. Astron. Soc.* **445** 3706–22
[36] Harrison E R 1970 Fluctuations at the threshold of classical cosmology *Phys. Rev.* D **1** 2726–30
[37] Zeldovich Y B 1972 A hypothesis, unifying the structure and the entropy of the Universe *Mon. Not. R. Astron. Soc.* **160** 1P
[38] Ade P A R *et al* (Planck Collaboration) 2016 Planck 2015 results. XX. Constraints on inflation *Astron. Astrophys.* **594** A20
[39] Wagstaff J M, Banerjee R, Schleicher D and Sigl G 2014 Magnetic field amplification by the small-scale dynamo in the early universe *Phys. Rev.* D **89** 103001
[40] Knollmüller J, Steininger T and Enßlin T A 2017 Inference of signals with unknown correlation structure from nonlinear measurements (arXiv e-prints)
[41] Vazza F, Brüggen M, Gheller C, Hackstein S, Wittor D and Hinz P M 2017 Simulations of extragalactic magnetic fields and of their observables *Class. Quantum Grav.* **34** 234001
[42] Federrath C 2016 Magnetic field amplification in turbulent astrophysical plasmas *J. Plasma Phys.* **82** 535820601
[43] Shukurov A 2004 Introduction to galactic dynamos (arXiv Astrophysics e-prints)
[44] Brandenburg A, Kahniashvili T, Mandal S, Pol A R, Tevzadze A G and Vachaspati T 2017 The dynamo effect in decaying helical turbulence (arXiv e-prints)
[45] Brandenburg A 2018 Advances in mean-field dynamo theory and applications to astrophysical turbulence (arXiv e-prints)
[46] Górski K M, Hivon E, Banday A J, Wandelt B D, Hansen F K, Reinecke M and Bartelmann M 2005 HEALPix: a framework for high-resolution discretization and fast analysis of data distributed on the sphere *Astrophys. J.* **622** 759–71
[47] Cabral B and Leedom L C 1993 Imaging vector fields using line integral convolution *Proc. of the 20th Annual Conf. on Computer Graphics and Interactive Techniques* (New York: ACM) pp 263–70
[48] Oppermann N *et al* 2012 An improved map of the Galactic Faraday sky *Astron. Astrophys.* **542** A93
[49] Waelkens A, Jaffe T, Reinecke M, Kitaura F S and Enßlin T A 2009 Simulating polarized Galactic synchrotron emission at all frequencies. The Hammurabi code *Astron. Astrophys.* **495** 697–706
[50] Beresnyak A and Miniati F 2016 Turbulent amplification and structure of the intracluster magnetic field *Astrophys. J.* **817** 127
[51] Beck A M, Hanasz M, Lesch H, Remus R-S and Stasyszyn F A 2013 On the magnetic fields in voids *Mon. Not. R. Astron. Soc.* **429** L60–4
[52] Subramanian K, Narasimha D and Chitre S M 1994 Thermal generation of cosmological seed magnetic fields in ionization fronts *Mon. Not. R. Astron. Soc.* **271** L15–8
[53] Subramanian K, Shukurov A and Haugen N E L 2006 Evolving turbulence and magnetic fields in galaxy clusters *Mon. Not. R. Astron. Soc.* **366** 1437–54
[54] Davis A-C, Lilley M and Törnkvist O 1999 Relaxing the bounds on primordial magnetic seed fields *Phys. Rev.* D **60** 021301